# Spinel-based ceramic membranes coupling solid sludge recycling with oily wastewater treatment

Chen, Mingliang; Zhu, Li; Chen, Jingwen; Yang, Fenglin; Tang, Chuyang Y.; Guiver, Michael D.; Dong, Yingchao

**DOI**
10.1016/j.watres.2019.115180

**Publication date**
2020

**Document Version**
Accepted author manuscript

**Published in**
Water Research

# Supporting information

## Spinel-based Ceramic Membranes Coupling Solid Sludge Recycling with Oily Wastewater Treatment

Mingliang Chen[a,b], Li Zhu[c], Jingwen Chen[a], Fenglin Yang[a], Chuyang Y. Tang[d], Michael D. Guiver[e], Yingchao Dong[a,*]

[a] Key Laboratory of Industrial Ecology and Environmental Engineering (Ministry of Education, MOE), School of Environmental Science and Technology, Dalian University of Technology, Dalian 116024, China

[b] Department of Sanitary Engineering, Faculty of Civil Engineering and Geosciences, Delft University of Technology, P.O. Box 5048, 2600 GA Delft, The Netherlands

[c] Engineering Research Center of Environmental Materials and Membrane Technology of Hubei province, School of Materials Science and Engineering, Wuhan Institute of Technology, Wuhan, P. R. China

[d] Department of Civil Engineering, The University of Hong Kong, Pokfulam, Hong Kong S.A.R., China

[e] State Key Laboratory of Engines, and Collaborative Innovation Center of Chemical Science and Engineering (Tianjin), Tianjin University, Tianjin 300072, P R China

***Corresponding authors:***

Dr. Yingchao Dong, Professor
Key Laboratory of Industrial Ecology and Environmental Engineering (Ministry of Education, MOE), School of Environmental Science and Technology, Dalian University of Technology, Dalian 116024, China
Tel: +86-411-84706328 E-mail: ycdong@dlut.edu.cn

## S1. Preparation of hollow fiber ceramic membranes

**Table S1**

Chemical composition (wt. %) of calcined bauxite measured by semi-quantitative XRF

| Materials | Chemical composition (wt. %) | | | | | | | | | | |
|---|---|---|---|---|---|---|---|---|---|---|---|
| | $Al_2O_3$ | $SiO_2$ | $TiO_2$ | $Fe_2O_3$ | MgO | CaO | $K_2O$ | $SO_3$ | $P_2O_5$ | $Na_2O$ | others |
| Calcined bauxite | 83.49 | 8.76 | 3.54 | 2.30 | 0.14 | 0.17 | 0.06 | 0.05 | 0.20 | 0.14 | 0.07 |

The loss on ignition of calcined bauxite is 1.09 wt. %

### *S1.1. Membrane fabrication*

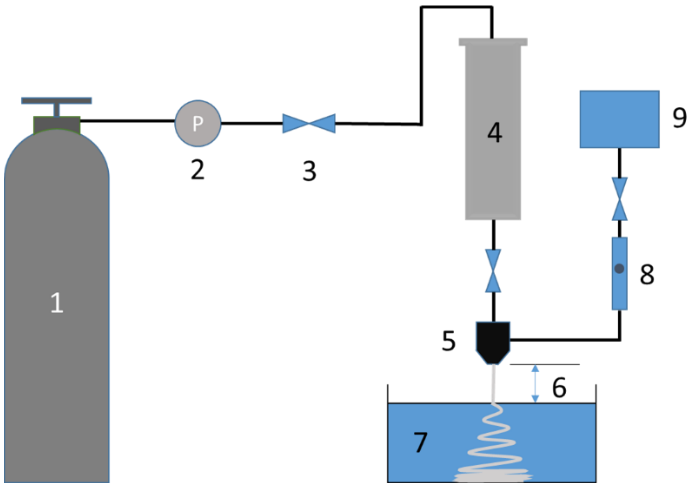


**Fig. S1.** Schematic diagram of experimental set-up for dry-wet spinning fabrication of hollow fiber membrane (1. Nitrogen cylinder, 2. Pressure gauge, 3. Valve, 4. Stainless reservoir, 5. Spinneret, 6. Air gap, 7. External coagulant, 8. Rotameter, 9. Internal coagulant)

The spinel-based HFCMs were prepared by a dry-wet spinning technique (Fig. S1), involving immersion-induced phase inversion and drying-sintering processes. Polyethersulfone (PES) was first dissolved in N-methyl-2-pyrrolidone (NMP) solvent at a PES/ NMP mass ratio of 1/4, then 3 g (1.5 wt. %) polyvinylpyrrolidone (PVP), moderating the solution viscosity, was added into the polymer solution under vigorous stirring for 6 h until a homogenous polymer mixture solution was formed. The ball-milled bauxite and nickel oxide mixture powder, based on a molar ratio of Ni/Al = 1/4, were added into the polymer solution and then wet-ball-milled for 48 h to ensure that the ceramic powders were well-dispersed. A molar ratio of Ni/Al = 1/2 was studied to semi-quantitatively analyze each phase content present in the samples. The prepared suspensions were then transferred to a gas tight reservoir and degassed under vacuum for 30 min at room temperature (25 °C).

The degassed spinning suspension was immediately introduced into a stainless steel reservoir and subsequently pressurized with nitrogen gas, and then the fiber was extruded through a tube-in-orifice spinneret (outer diameter 2.5 mm, inner diameter 1.3 mm) into external coagulant with different air-gap distances. Deionized (DI) water was used the internal coagulant at a flow rate of 20 mL·min$^{-1}$. The external coagulants used in this work are the mixtures of tap-water and ethanol with different ethanol volumes (0 %, 30 %, 60 % and 90 %) (Table S2).

**Table S2**

Suspension compositions and dry-wet spinning parameters for Fibers 1-8

| Fiber no. | Solid state loading (wt.%) | Bore fluid flow rate (mL·min$^{-1}$) | Air-gap (cm) | Internal coagulant | External coagulant (water/ethanol) |
|---|---|---|---|---|---|
| 1 | 50 | 20 | 15 | Deionized water | 100/0 |
| 2 | 55 | 20 | 15 | Deionized water | 100/0 |
| 3 | 60 | 20 | 15 | Deionized water | 100/0 |
| 4 | 60 | 20 | 10 | Deionized water | 100/0 |
| 5 | 60 | 20 | 3 | Deionized water | 100/0 |
| 6 | 60 | 20 | 15 | Deionized water | 70/30 |
| 7 | 60 | 20 | 15 | Deionized water | 40/60 |
| 8 | 60 | 20 | 15 | Deionized water | 10/90 |

The hollow fiber green bodies were immersed in the external coagulant bath overnight to allow completion of the phase inversion process. They were then rinsed with tap water in order to remove trace amounts of NMP. Afterwards, the fibers were dried at room temperature (25 °C), then sintered in air for 2 h at temperatures between 1200 °C and 1300 °C with an interval of

25 °C to produce robust porous HFCMs.

*S1.2. Membrane characterization*

The tests of three-point bending strength of sintered HFCMs were performed using a universal testing machine (AGS-X, Shimadzu Ltd., Japan). During the tests, the samples were placed on a span of 8 mm and were loaded at a crosshead speed of 0.02 $mm \cdot min^{-1}$ until fracture occurred. Each sample were repeated for twenty runs. The bending strength, $\sigma_f$, was calculated from the following equation:

$$\sigma_f = 8FLD/(\pi(D^4-d^4)) \qquad (1)$$

Where, F is the measured force at which fracture takes place (N), L, D and d are the span (8mm), the outer and inner diameters of the hollow fiber, respectively.

Pore size distribution was determined using a pore size distribution analyzer (Porometer 3G, Quantachrome Instruments, USA) based on a gas-liquid displacement method with nitrogen gas as the permeation medium.

$$r = 4\gamma\cos\theta/\Delta P \qquad (2)$$

where r (μm) is the diameter of the pore, $\Delta P$ (MPa) is the applied pressure difference, $\gamma$ (mN/m) is the surface tension of the liquid and $\theta$ is the contact angle.

The Fourier-transform infrared spectroscopy (FTIR) was recorded with an infrared spectrometer (Bruker EQUINOX55, Germany) to analyze the functional groups present in sintered spinel-based membranes. The X-ray photoelectron spectroscopy (XPS) measurements were performed on an electron spectrometer (ESCALAB 250Xi, ThermoFisher, US) for multi-technique surface analysis systems, with Al Kα photons used as a source and operated at a constant power of 300 W. The core level binding energies of the different peaks were normalized by setting the bonding energy of C1s peaks for C-C bonds at 284.8 eV. The structure and morphology of the formed spinel was observed through transmission electron microscopy (TEM, JEM-2010(HR), JEOL, Japan) operated at 200 kV. To study microtextures, diffraction patterns (DPs) were collected using the selected area electron diffraction (SAED) technique.

Pure water flux of the HFCMs was characterized by a laboratory-made crossflow filtration apparatus. The apparatus was operated at a very low constant trans-membrane pressure of 0.1 bar with different feed velocities ranging from 0.14 $m \cdot s^{-1}$ to 0.73 $m \cdot s^{-1}$. Before starting the measurements of permeate flux, all samples were ultrasonically cleaned with ethanol for 5 min.

*S1.3. Stabilization of O/W emulsions*

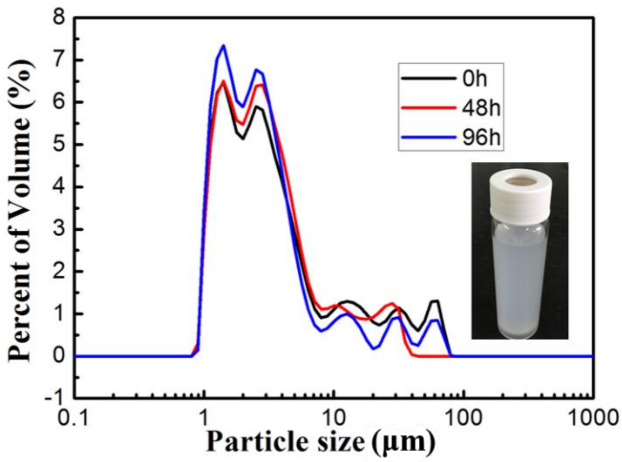


**Fig. S2.** The size distributions of emulsified oil droplets in the feed solutions after 0, 48, and 96 h static storage.

In order to illustrate the stability of O/W emulsions prepared in our work, the size distributions of emulsified oil droplets after 0, 48, and 96 h static storing were measured using a laser particle size analyzer, as shown in Fig. S2. It is clear that the prepared O/W emulsions were highly stable for MF separation experiments, as the size distributions of emulsified oil droplets are quite similar even after 96 h static storage, indicating a good dispersion and stable state. In addition, the majority of the size of oil droplets in the emulsions are in the range of 1~10 μm, which meets the classification criteria for industrial O/W emulsified wastewaters.

*S1.4. O/W emulsion separation by HFCMs*

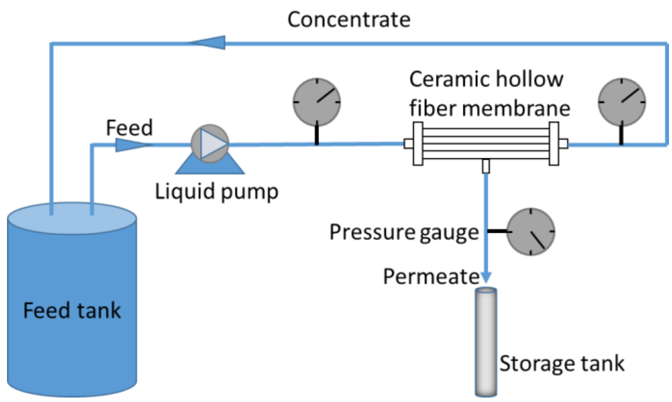


**Fig. S3.** Schematic diagram of experimental setup for membrane-based process treatment of O/W emulsions.

## S2 Thermal conversion of $NiAl_2O_4$

### *S2.1. Thermal Conversion Mechanism of $NiAl_2O_4$*

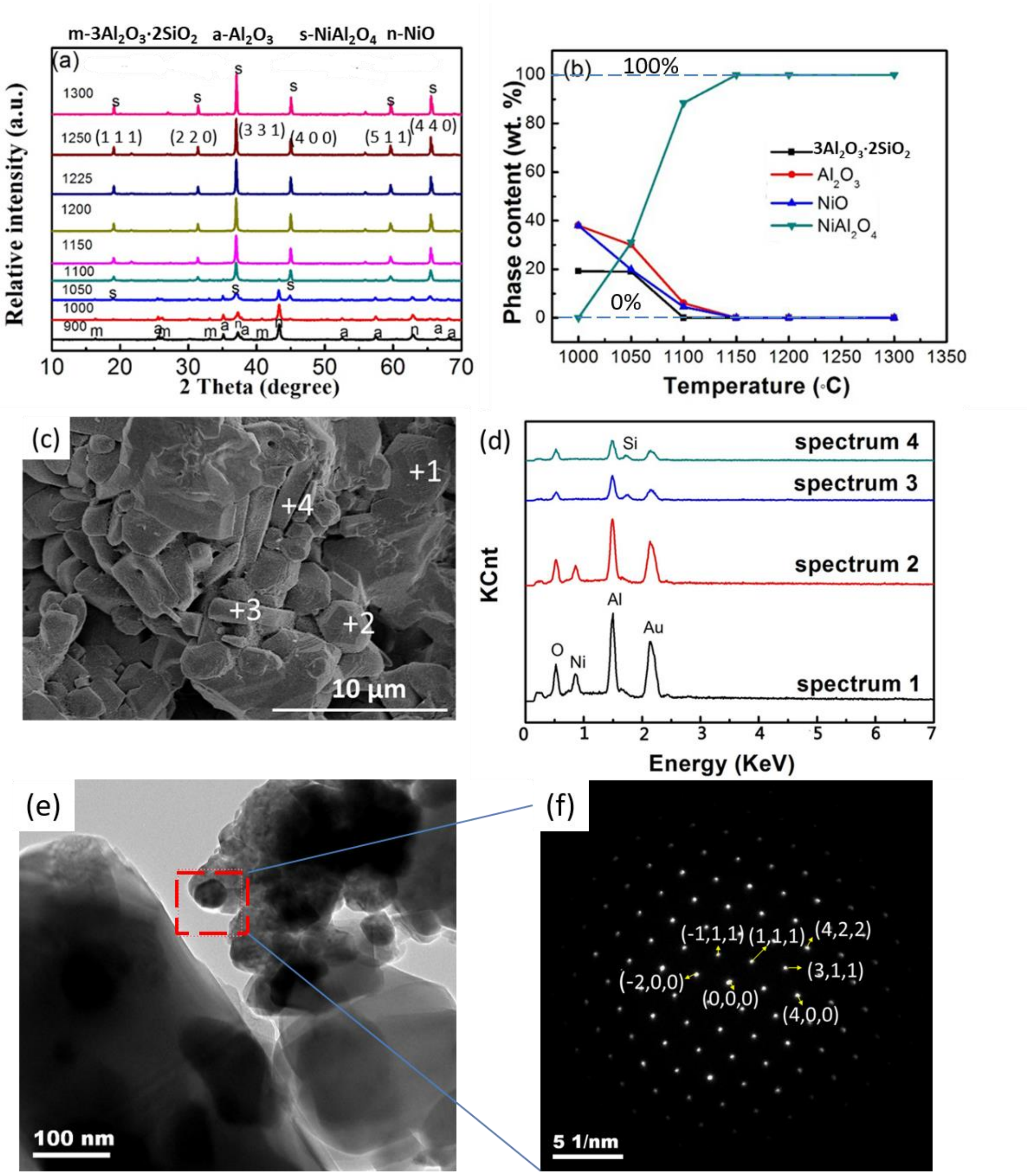


**Fig. S4.** (a) XRD patterns and (b) quantified phase content of the spinel-based hollow fiber ceramic membranes (NiAl2) sintered at various temperature from 900 to 1300 °C for 2 h, $3Al_2O_3{\cdot}2SiO_2$ (PDF #83-1881), α-$Al_2O_3$ (PDF#99-0036), $NiAl_2O_4$ (PDF#81-0718) and NiO (PDF#44-1159), (c) SEM image and (d) EDS spectra of the spinel-based membrane (NiAl4) sintered at 1400 °C for 2 h, after 15 wt. % HF solution etching for 30 min, (e) TEM image of the spinel-based membrane (NiAl4) sintered at 1250 °C, (f) SAED patterns of a spinel crystal with octahedral morphology as indicated by red dash line in Fig. S4e.

Table S3

EDS analysis of the NiAl4 membrane sintered at 1400 °C for 2 h after leaching at 15 wt. % HF solution for 30 min.

| Position | at. % | | | Molar ratio | | Main phase |
|---|---|---|---|---|---|---|
| | Al | Ni | Si | Al/Si | Al/Ni | |
| Spectrum1 | 47.14 | 20.35 | - | - | 2.3 | spinel |
| Spectrum2 | 49.22 | 18.91 | - | - | 2.6 | spinel |
| Spectrum3 | 55.18 | - | 13.75 | 4 | - | mullite |
| Spectrum4 | 50.04 | - | 12.8 | 3.9 | - | mullite |

*S2.2. Acidic stability of $NiAl_2O_4$*

To evaluate the product leachability under prolonged acidic exposure, the NiO, NiAl2 and NiAl4 samples were tested following a modified method from the U.S. EPA Toxicity Characteristic Leaching Procedure (TCLP) (Shih and Tang, 2011) by using acetic acid (pH 2.9) solution as the leaching fluid. Each leaching vial was filled with 40 mL of TCLP extraction fluid and 2 g of ground powder of NiO and prepared NiAl2 and NiAl4 spinel-based HFCMs. The leachates were filtered through 0.2 μm syringe filters and the concentrations of metal ions were determined by atomic absorption spectrometer (Solaar M6, Thermo, USA).

The stability of NiAl4 and NiAl2 phase is much higher than that of NiO (Fig. S5). As shown, the concentration of leached nickel ion in NiO sample increases sharply with the leaching time. After 16 days leaching, its nickel ion concentration was as high as 516 $mg \cdot L^{-1}$ and even maintains a rising trend. In contrast, the nickel ion leached from NiAl2 and NiAl4 are found to be much lower than that from NiO. Within 24 h of leaching, its concentration is only 9.17 $mg \cdot L^{-1}$ and 5.14 $mg \cdot L^{-1}$ and then increases with leaching time very slowly. Even after 16 days leaching, the nickel ion concentration is still very low and the impurity ions from bauxite, such as titanium and iron ions, are hard to be detected. These results not only illustrate the successful incorporation of nickel into bauxite but also the effective stabilization of nickel into the more stable spinel phase $NiAl_2O_4$, to resist the acidic attack.

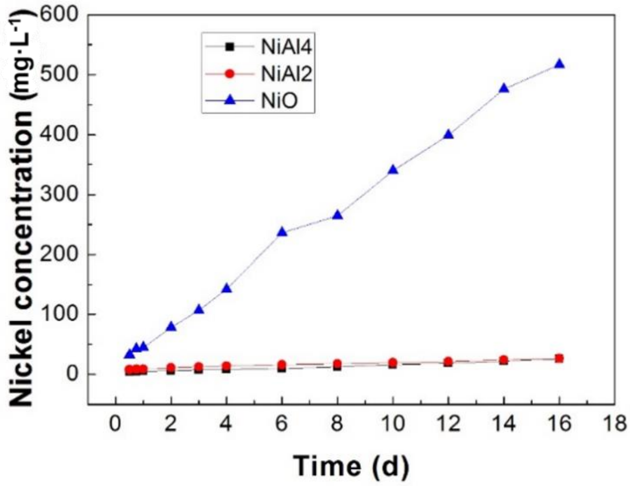


**Fig. S5.** Concentration of nickel ion in the NiO and NiAl2, NiAl4 (sintered at 1400 °C) leachates.

**Table S4**

Comparison of raw materials for nickel-laden solid state wastes stabilization.

| Raw materials | Price (\$/t)[1] | Full transformation temperature (°C) |
|---|---|---|
| Bauxite | 150-200 | 1200 |
| Alumina | 520-540 | 1400 |
| Kaolinite | 300-360 | 1350 |

1-adapted from Alibaba.com

**Table S5**

Comparison of formation temperature and stability between nickel aluminate spinel phase in this work and those reported in the literatures.

| Heavy metal | Starting materials | Targeted phase | Formation temperature (°C) | Leachability ($mg \cdot L^{-1}$) | Refs |
|---|---|---|---|---|---|

| | | | | | |
|---|---|---|---|---|---|
| Ni | NiO + bauxite | $NiAl_2O_4$ | 1000~1200 | 26 | This work |
| Ni | NiO + γ-$Al_2O_3$ | $NiAl_2O_4$ | 1100~1400 | 84 | (Shih et al., 2006b) |
| Ni | NiO + kaolinite | $NiAl_2O_4$ | 1150~1400 | 20 | (Shih et al., 2006b) |
| Cu | CuO + bauxite | $CuAl_2O_4$ | 900~1060 | 213 | (Li et al., 2015a) |
| Cu | CuO + mullite | $CuAl_2O_4$ | 950~1050 | <200 | (Tang et al., 2011a) |
| Cu | CuO + kaolin | $CuAl_2O_4$ | 900~1050 | <200 | (Tang et al., 2011a) |
| Zn | ZnO + bauxite | $ZnAl_2O_4$ | 1000~1300 | 15 | (Li et al., 2015b) |
| Zn | ZnO + corundum | $ZnAl_2O_4$ | 850~1350 | 2.7 | (Tang et al., 2011b) |

The formation temperature and stability of nickel aluminate spinel phase prepared in this work are compared with those reported in the literature, as presented in Table S4. For the stabilization of the same heavy metals, the stable temperature ranges at which they exist are close to each other, and are independent of the raw materials used. As both bauxite and kaolinite transform to mullite and corundum/cristobalite under thermal treatment, silica does not react with nickel, and the only incorporation mechanism is through the reaction between NiO and mullite or $Al_2O_3$ (Shih et al., 2006b). However, the stability of spinel phase shows slight differences. For example, the leaching of Cu ions from CuO-bauxite, CuO-mullite and CuO-kaolinite systems is much higher than that of nickel and zinc spinel due to the relatively lower stability of copper spinel (Tang et al., 2011a; Dong et al., 2010). The $NiAl_2O_4$ spinel phase stable existence temperature range in this work is quite similar with two other $NiAl_2O_4$ spinel phases reported in the literature and its nickel ion leaching concentration is only 26 $mg{\cdot}L^{-1}$, even after half a month, which is a little higher than that of the NiO-kaolinite system ($20\ mg\cdot L^{-1}$), but much lower than that of the NiO-$\gamma$-$Al_2O_3$ system ($84\ mg\cdot L^{-1}$). The reason is possibly due to enhanced spinel crystallization and robust grain boundaries promoted by the silica flux in NiO-kaolinite and NiO-bauxite systems (Shih et al., 2006a). By comparison, both the market price of bauxite mineral and stable existence temperature of nickel-based spinel are lower than that of alumina and kaolinite (Table S5), indicating that bauxite is an efficient and cost-effective material for stabilization of nickel-laden solid-state wastes.

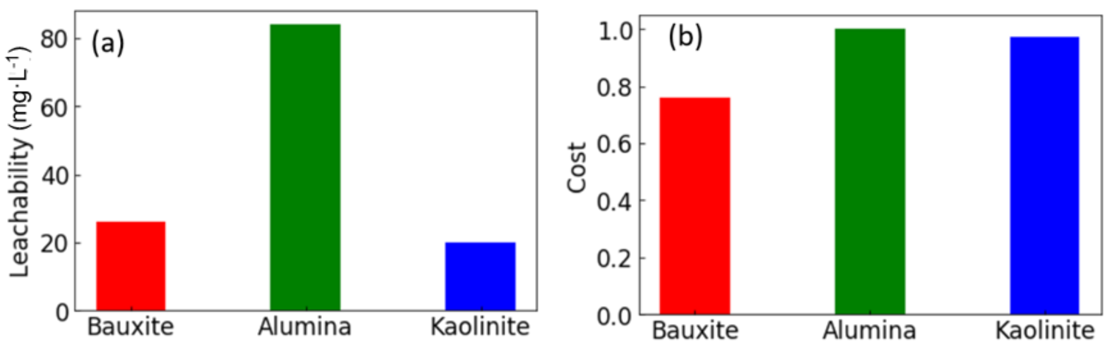


**Fig. S6.** Acidic leachability (a) and cost comparison (b) of Ni-based spinel stabilized by bauxite (this work), alumina, and kaolinite, reported in the open literature (Shih et al. 2006b).

## S3. Rational structure design of ceramic membranes

*S3.1. Effect of solid-state loading*

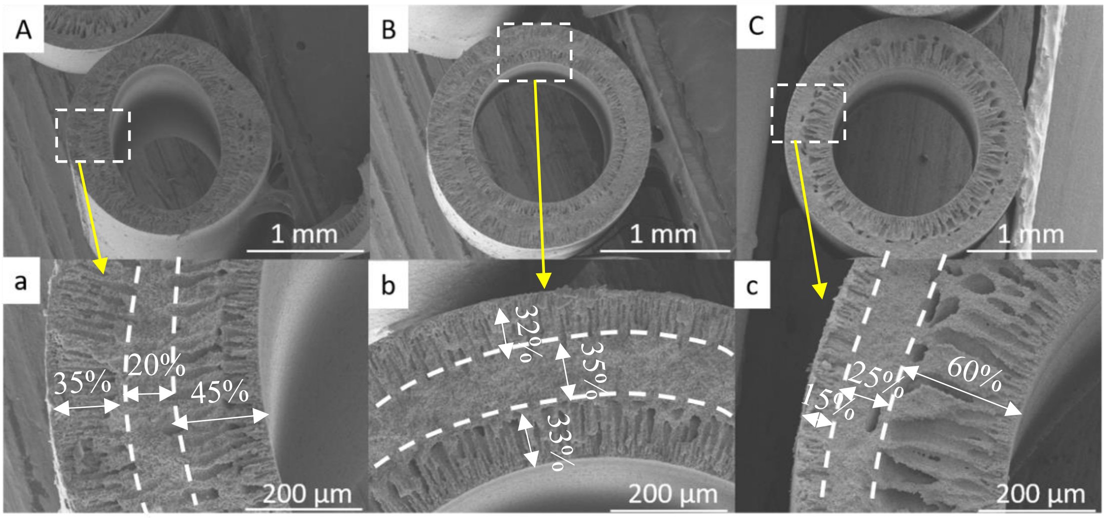


**Fig. S7.** Cross sectional SEM images of fibers 1, fiber 2 and fiber 3 sintered at 1250 °C for 2 h with different solid state loadings: (A, a) 50 wt. %, (B, b) 55 wt. %, (C, c) 60 wt. %, at a fixed air-gap distance of 15 cm and tap-water as external coagulant, respectively.

With ceramic suspensions consisting of 50 wt. %, 55 wt. % and 60 wt. % solid state loadings, the spinel-based HFCMs were wet-dry and spun at an air gap distance of 15 cm and a fixed bore fluid rate of 20 $mL \cdot min^{-1}$, followed by sintering at 1250 °C for 2 h. Cross sectional SEM images of the fiber membranes are shown in Fig. S7. An asymmetric sandwich porous structure was formed for all the spinel hollow fiber membranes with inner and outer finger-like macro-void structures enhancing permeability and with sponge-like region providing the majority of the mechanical strength and size-exclusion separation function (Zhu et al., 2016). However, deformation of the lumen was observed when the ceramic loading was 50 wt. % (Fig. S7A). With further increasing the ceramic loading to 55 wt. % (Fig. S7B) and 60 wt. % (Fig. S7C), both fibers have regular inner and outer shape. When comparing the cross-sectional SEM images of fiber2 and fiber3, a structure with much longer and bigger inner finger-like macro-voids is observed for fiber3, while the thickness of outer finger-like macro-voids and sponge-like region is reduced. This indicates that solid-state loadings play a crucial role in the formation of regular lumen as well as the distribution and ratio of finger-like macro-voids and sponge-like regions. When increasing solid state loadings, the viscosity of spinning suspension was improved (Luiten-Olieman et al., 2011), which lowered the exchange rate of solvent and non-solvent. As a result, the formation of outer finger-like structure was suppressed and thinner outer finger-like macro-voids were observed, shown in Fig. S7c.

*S3.2. Effect of air-gap distance*

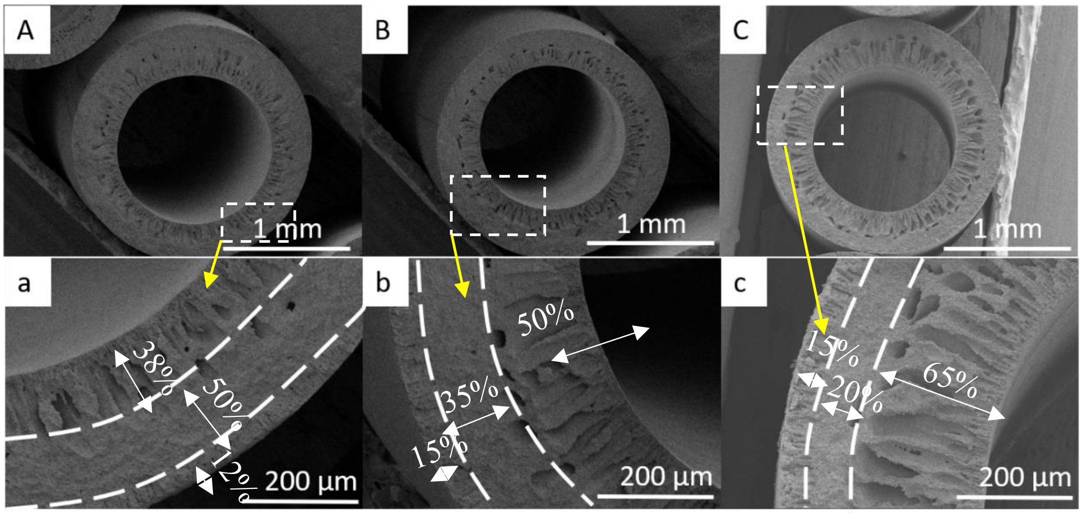


**Fig. S8.** Cross sectional SEM images of fibers 3, 4 and 5 sintered at 1250 °C for 2 h with different air gap distances: (A, a) 3 cm, (B, b) 10 cm, (C, c) 15 cm, at a fixed solid-state loading of 60 wt. % and tap-water as the external coagulant, respectively.

Fig. S8 shows spinel-based HFCMs spun with air gap distances of 3 cm, 10 cm and 15 cm, a solid-state loading of 60 wt. % and a fixed bore fluid rate of 20 mL·min$^{-1}$, followed by sintering at 1250 °C for 2 h. All fibers have a structure consisting of a sponge-like region as well as the inner and outer finger-like macro-voids. However, the distribution and ratio of finger-like macro-voids and sponge-like regions varied with the air gap distances. With the increase of air gap distance, the thickness of the sponge-like region was gradually decreased, while the length of the inner finger-like macro-voids increased significantly (Kingsbury et al., 2010; Kingsbury and Li, 2009). When the fiber was spun into a non-solvent bath (tap water) with 3 cm air-gap distance (Fig. S8a), the finger-like macro-voids extend from the inner fiber surface across approximately 38% of the fiber cross-section, which is much longer than finger-like macro-voids originating from the outer fiber surface with only 12%. A central sponge-like region between the inner and outer finger-like voids was estimated to be about 50% of the fiber cross-section.

The size and length of macro-voids at the inner edge are further increased when the air-gap distance is increased to 10 cm, the finger-like voids extended from the inner surface across approximately 50% of the fiber cross-section, while the sponge-like region was reduced, only occupying about 35% of the fiber cross-section (Fig. S8b). The thickness of sponge-like region (20%) between the inner and outer finger-like voids are further reduced when the air-gap distance is increased to 15 cm (Fig. S8c). When the fiber was extruded from the spinneret, rapid precipitation at the inner fiber walls occurred, resulting in long finger-like voids, before it was immersed in non-solvent coagulation bath. Therefore, the increase of air-gap induced more rapid precipitation, which occurred at the inner fiber walls and the presence of ambient moisture in the air caused an increase in viscosity at the outer surface of the fiber, which inhibit the formation of outer finger-like macro-voids and favor the growth of inner finger-like pores (Meng et al., 2016).

*S3.3. Effect of external coagulant*

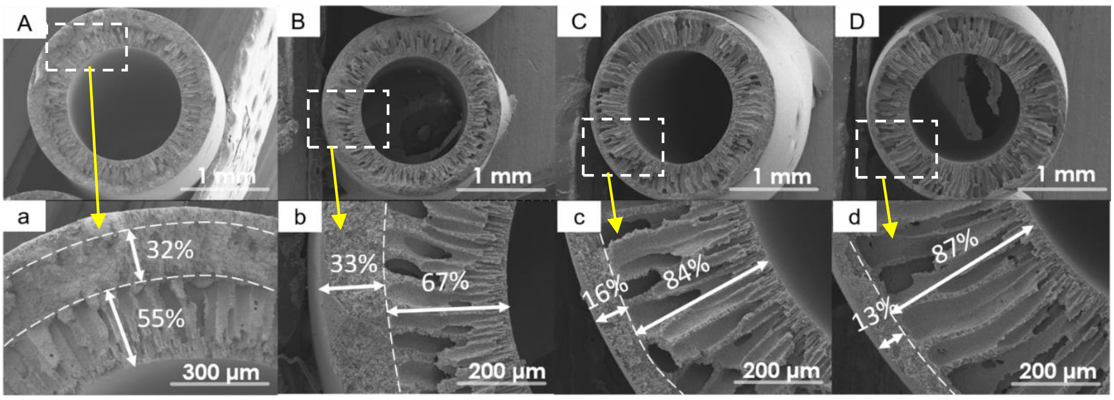


**Fig. S9.** Cross sectional SEM images of fibers 3, 6 and 8 prepared with different volumes of ethanol as external coagulants: (A, a) 0 vol%, (B, b) 30 vol%, (C, c) 60 vol%, (D, d) 90 vol% at a fixed air-gap distance of 15 cm and solid-state loading of 60 wt. %, respectively.

To investigate the effect of external coagulants on fiber morphology, different volumes of ethanol/water mixture solutions were used as external coagulants, with other conditions being the same. The inner and outer finger-like macro-voids of the fiber prepared with water as the external coagulant account for approximately 55% and 13% of the fiber cross-section respectively (Fig. S9a), with the remaining 32% consisting of a sponge-like region. Addition of 30 vol. % of ethanol into the external coagulants results in an increase in finger-like macro-voids which occupy 67% of the fiber cross-section (Fig. S9b). Although the thickness of the sponge-like region was not reduced, the finger-like voids appeared to migrate toward to the outer surface. With a further increase of volume percent of ethanol up to 60% and above, the cross-section of the fiber precursors are mainly composed of long and large inner finger-like macro-voids and thin sponge-like region, along with the elimination of outer finger-like macro-voids (Figs. S9c and S9d). A similar phenomenon has been also reported by Zhang et al. (Zhang et al., 2015) , who prepared the YSZ hollow fibers with ethanol as external coagulant and finger-like macro-voids extended from the inner wall across approximately 90% of the fiber cross-section. These differences in microstructure of the fiber precursor could be attributed to the coagulation power of coagulant which influenced the cross-section structure formation of membranes significantly during phase inversion process. As the coagulation power increases, the polymer-solvent interaction is enhanced, and thus the precipitation rate is improved to form finger-like structures (Um et al., 2004). Compared with water, ethanol is a weak coagulant. Thus, when more ethanol was incorporated as the external coagulant, the precipitation of polymer was significantly inhibited at the outer surface of the fiber. In addition, using strong coagulant water as the internal coagulant at the inner side of the nascent fibers leads to the rapid precipitation of polymer. The presence of an air-gap distance of 15 cm further promotes extending the finger-like macro-voids toward to the outer side (Um et al., 2004; Wang et al., 2000). Thus, a structure with long and large finger-like macro-voids and a thin sponge-like region is formed.

Compared with the hollow fibers prepared using water as the external coagulant (sandwich structured HFCM (SS-HFCM), fiber 3), the highly asymmetric hollow fibers having long finger-like pore structured HFCM (LFS-HFCM) (fiber 7) prepared with 60% volume of ethanol as external coagulant are more beneficial for the development of separation membranes as the thin outer sponge-like region reduces mass transfer resistance effectively during the filtration process (Burggraaf, 1996).

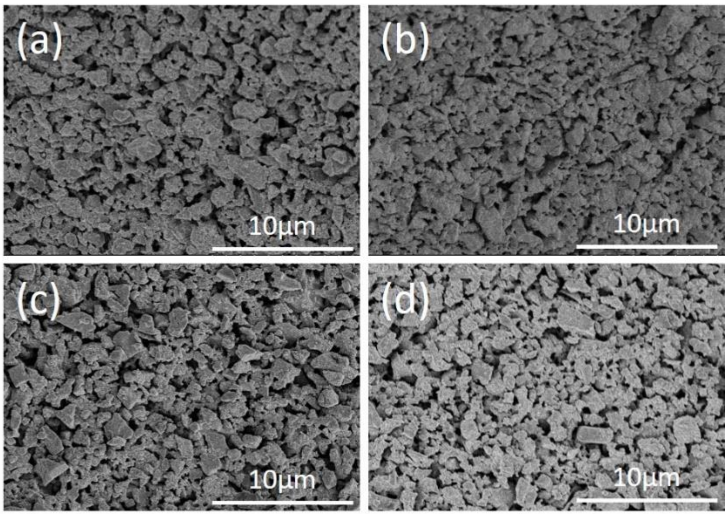


**Figure. S10.** Inner and outer surface SEM images of SS-HFCM and LFS-HFCM sintered at 1250 °C: (a) inner surface of SS-HFCM, (b) outer surface of SS-HFCM, (c) inner surface of LFS-HFCM, (d) outer surface of LFS-HFCM.

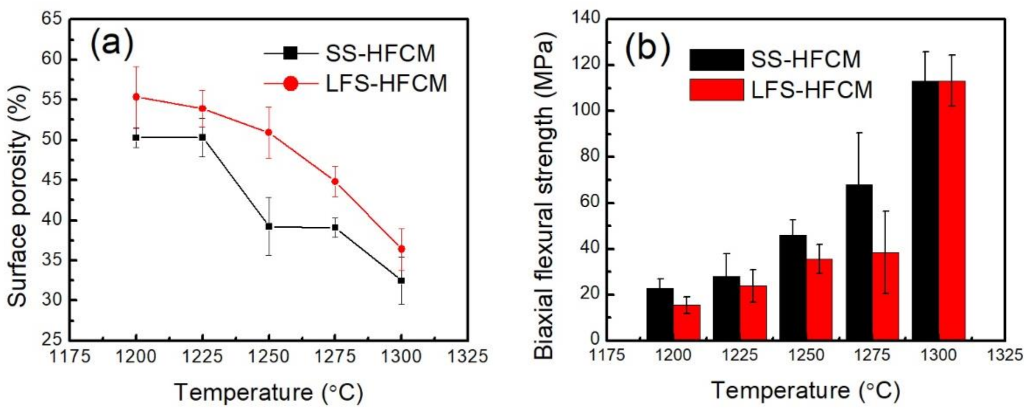


**Fig. S11.** (a) Surface porosity and (b) biaxial flexural strength of SS-HFCM and LFS-HFCM sintered from 1200 to 1300 °C

Fig. S11 shows the surface porosity and mechanical strength of SS-HFCM and LFS-HFCM after sintering at various temperatures (1200-1300 °C). The surface porosity of SS-HFCM and LFS-HFCM both decrease with sintering temperature, while LFS-HFCM always has a higher surface porosity than SS-HFCM. A reverse phenomenon was observed for the bending strength of both fibers, which increases with the sintering temperatures. SS-HFCM always has a higher strength than LFS-HFCM, except at 1300 °C. As the sponge-like regions provide the majority of the mechanical strength of hollow fiber membranes, SS-HFCM has a thicker sponge-like region than LFS-HFCM and a higher mechanical strength is observed for SS-HFCM. When the sintering temperature increases up to 1300 °C, a severe densification process occurs, resulting in a dramatic increase in mechanical strength for both fibers, which is independent of the fiber structures.

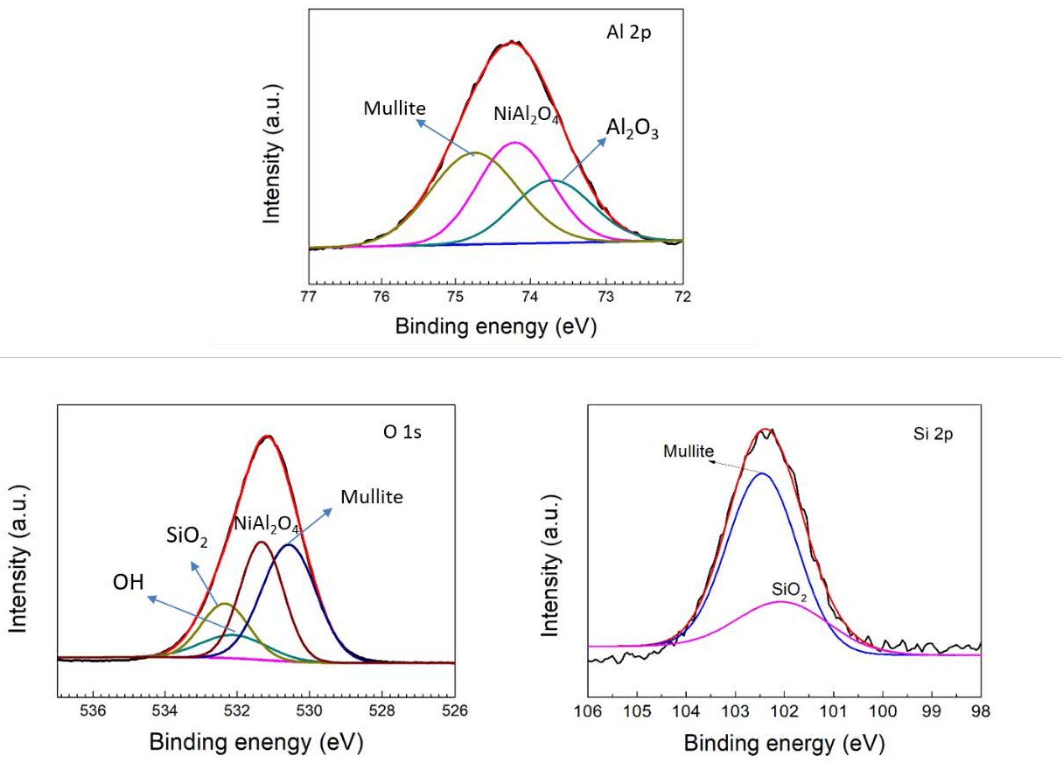


**Fig. S12.** XPS spectra of O 1s, Al 2p and Si 2p of LFS-HFCM sintered at 1250 °C

## S4 Oil-in-water emulsion separation

### *S4.1. Introduction of membrane fouling models*

To analyze cross-flow microfiltration flux decline profiles of O/W emulsions, four fouling models, namely cake filtration model, intermediate pore blocking, standard pore blocking model and complete pore blocking model have been used (Kumar et al., 2015; Vasanth et al., 2013; Salahi et al., 2010; Nandi et al., 2010). The cake filtration model is applied to the situation where particles larger than the average pore size deposit on the membrane surface, thus forming a cake filtration layer, which provide an additional porous barrier to the permeating liquid. Intermediate pore blocking occurs when the solute particle sizes are equivalent to the membrane pore sizes. Using this model, the membrane pores are considered as not necessarily blocked by the solute particles. Standard pore blocking is caused by the non-uniformity of pore paths and pore blocking inside the membrane pore occurs when the solute particle sizes are smaller than the membrane pores. In complete pore blocking, the sizes of solute particle are bigger than the membrane pore and thus pore blocking usually occurs on the membrane surface rather than within the membrane pore. The four fouling models are expressed by the following linearized equations of the membrane flux (J) and time (t) (Hermia, 1982):

(a) Cake filtration: $J^{-2} = J_0^{-2} + k_c t$ (3)

(b) Intermediate pore blocking: $J^{-1} = J_0^{-1} + k_i t$ (4)

(c) Standard pore blocking: $J^{-0.5} = J_0^{-0.5} + k_s t$ (5)

(d) Complete pore blocking: $\ln (J^{-1}) = \ln (J_0^{-1}) + k_b t$ (6)

The fitting of the experimentally acquired permeate flux decline vs time data with any of above models is confirmed by comparing the coefficient of correlation ($R^2$) values coupled with positive combinations of slope and intercept values obtained from linear fit analysis. As a result, the model that represents experimental data with best fit $R^2$ is considered to indicate the pertinent fouling mechanism during cross flow microfiltration.

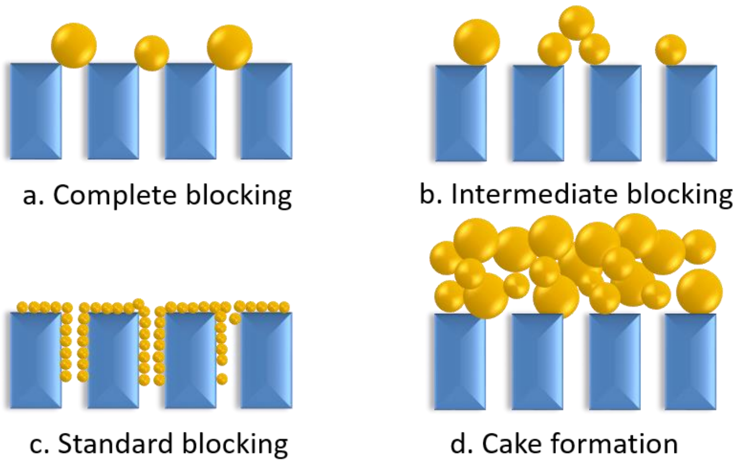


**Fig. S13.** Illustration of fouling mechanisms considered by the models.

To explain the results in a better way, we also have calculated Reynolds number (Re) at different cross-flow velocities (Table S7) using the following equation:

$$Re = \rho v d/\mu \tag{7}$$

Where ρ is the density of the fluid ($kg \cdot m^{-3}$), v is the velocity of the fluid with respect to the object ($m \cdot s^{-1}$), d is the inner diameter of the membrane tube (m), and μ is the dynamic viscosity of the fluid ($kg \cdot m^{-1} \cdot s^{-1}$).

**Table S6**

Summary of parameters associated with various pore blocking models at different cross-flow velocities for O/W emulsion separation.

| membrane | Cross-flow velocity ($m \cdot s^{-1}$) | Cake filtration | | | Intermediate pore blocking | | | Standard pore blocking | | | Complete pore blocking | | |
|---|---|---|---|---|---|---|---|---|---|---|---|---|---|
| | | $R^2$ | $k_c$ ($s \cdot m^{-2}$) | $J_0^{-2} \times 10^{-7}$ | $R^2$ | $k_i$ ($m^{-1}$) | $J_0^{-1} \times 10^{-3}$ | $R^2$ | $k_s$ ($s^{0.5} \cdot m^{0.5}$) | $J_0^{0.5} \times 10^{-1}$ | $R^2$ | $k_b$ ($s^{-1}$) | $\ln(J_0^{-1})$ |
| LFS-HFCM | 0.56 | 0.966 | 0.318 | 13.78 | 0.934 | 0.089 | 12.46 | 0.907 | 0.034 | 11.26 | 0.874 | 0.005 | 9.46 |
| LFS-HFCM | 1.12 | 0.988 | 0.248 | 5.03 | 0.955 | 0.091 | 8.27 | 0.925 | 0.039 | 9.25 | 0.887 | 0.007 | 9.08 |
| LFS-HFCM | 1.67 | 0.973 | 0.055 | 1.86 | 0.968 | 0.038 | 4.76 | 0.961 | 0.023 | 6.99 | 0.949 | 0.005 | 8.51 |

| | | | | | | | | | | | | | |
|---|---|---|---|---|---|---|---|---|---|---|---|---|---|
| SS-HFCM | 1.67 | 0.995 | 0.076 | 2.76 | 0.989 | 0.044 | 5.74 | 0.981 | 0.024 | 7.67 | 0.967 | 0.005 | 8.7 |

**Table S7**

Reynolds number at different cross-flow velocities.

| Cross-flow velocity ($m \cdot s^{-1}$) | Reynolds number (Re) | Flow patterns |
|---|---|---|
| 0.56 | 728 | Laminar flow |
| 1.12 | 1456 | Laminar flow |
| 1.67 | 2171 | Laminar–turbulent transition |

*S4.2. Cost and environmental risk assessment*

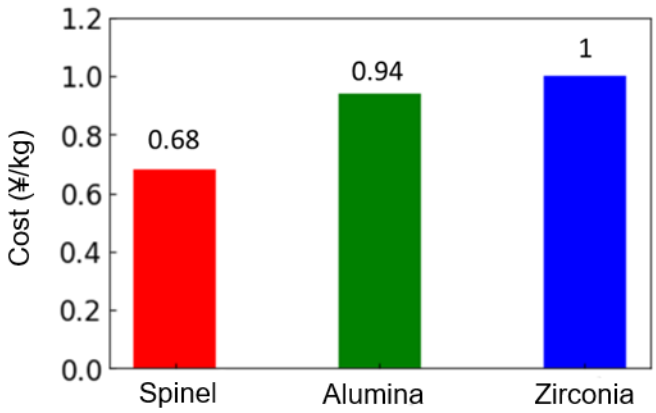


**Fig. S14.** Comparison of membrane fabrication cost based on consumption of raw materials and electricity during sintering.

The sintering temperature of spinel-based HFCMs in this study is much lower than of traditional ceramic membranes such as $Al_2O_3$ and $ZrO_2$. The cost analysis is based on the raw materials and energy consumption for membrane sintering. The spinel-based HFCMs has a lower fabrication cost than $Al_2O_3$ and $ZrO_2$ membranes due to cheaper raw materials and lower sintering temperatures. The stabilization cost using bauxite as precursors is also lower than those using alumina and kaolinite as precursors. Therefore, bauxite is a promising candidate raw material for both heavy-metal stabilization and membrane fabrication due to lower cost and outstanding separation performance in water treatment.

**Table S8**

The concentrations of some typical metal-ions in the permeate after membrane separation operation of oil-in-water emulsion

| Concentration ($\mu g \cdot L^{-1}$) | Al | Ca | Fe | K | Mg | Na | Ni | Ti |
|---|---|---|---|---|---|---|---|---|
| This work | 13.7 | 77.1 | --- | 69.4 | 14.6 | 144.7 | 0.7 | --- |
| Drinking water criterion (WHO) | 900 | - | 0.3 | - | - | 5000 | 70 | - |

--- non-detected

**S5. Preliminary extension to other spinel systems**

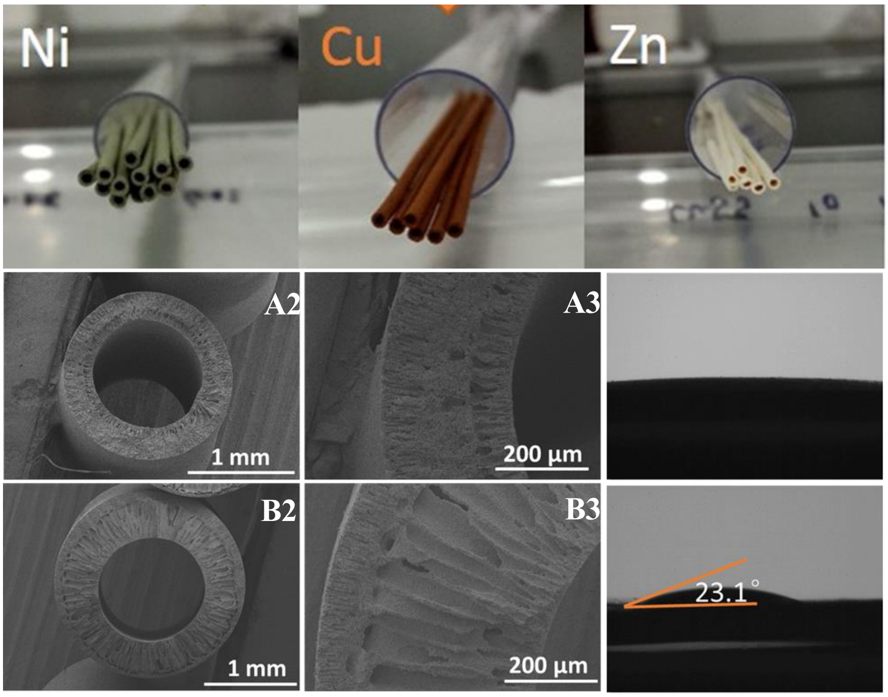


**Fig. S15.** Photos of NiAl2, CuAl2 and ZnAl2 hollow fiber ceramic membranes and cross sectional SEM images CuAl2 (A1, A2) and ZnAl2 (B1, B2) sintered at 1000 °C and 1400 °C for 2 h respectively, (A3) water contact angle of CuAl2 sintered at 1000 °C and (B3) water contact angle of ZnAl2 sintered at

1400 °C.

The study of recycling of nickel-laden wastewater sludge for rational fabrication of spinel-based ceramic membranes is not only an efficient way to highly efficiently stabilize heavy metals in wastewater sludge into much more stable spinel phase, but also to provide a new avenue for developing high performance robust membranes for water treatment. Furthermore, this strategy is not limited to nickel and could also extend to other heavy metals in wastewater sludge such as copper and zinc. The CuAl2 and ZnAl2 membranes prepared via the protocol proposed in this study also show a good asymmetric structure and have a water contact angle of 0° and 21°, respectively (Fig. S15), indicating a great potential for water treatment due to their excellent hydrophilicity.

## References


Burggraaf, A.J., 1996. Membrane Science and Technology, pp. 21-34, Elsevier.

Dong, Y., Hampshire, S., Lin, B., Ling, Y. Zhang, X., 2010. High sintering activity Cu–Gd co-doped $CeO_2$ electrolyte for solid oxide fuel cells. J. Power Sources 195 (19), 6510-6515.

Hermia, J., 1982. Constant pressure blocking filtration laws-application to power-law non-Newtonian fluids. Chem. Eng. Res. Des. 60, 183-187.

Kingsbury, B.F., Li, K., 2009. A morphological study of ceramic hollow fiber membranes. J. Membr. Sci. 328 (1-2), 134-140.

Kingsbury, B.F., Wu, Z., Li, K., 2010. A morphological study of ceramic hollow fiber membranes: A perspective on multifunctional catalytic membrane reactors. Catal. Today 156 (3-4), 306-315.

Kumar, R.V., Ghoshal, A.K., Pugazhenthi, G., 2015. Elaboration of novel tubular ceramic membrane from inexpensive raw materials by extrusion method and its performance in microfiltration of synthetic oily wastewater treatment. J. Membr. Sci. 490, 92-102.

Li, L., Dong, X., Dong, Y., Zheng, Y.-M., Zhu, L., Liu, J., 2015a. Thermal conversion of hazardous metal copper via the preparation of $CuAl_2O_4$ spinel-based ceramic membrane for potential stabilization of simulated copper-rich waste. ACS Sustain. Chem. Eng. 3 (11), 2611-2618.

Li, L., Dong, X., Dong, Y., Zhu, L., You, S.-J., Wang, Y.-F., 2015b. Incorporation of zinc for fabrication of low-cost spinel-based composite ceramic membrane support to achieve its stabilization. J. Hazard. Mater. 287, 188-196.

Luiten-Olieman, M.W., Winnubst, L., Nijmeijer, A., Wessling, M., Benes, N.E., 2011. Porous stainless steel hollow fiber membranes via dry–wet spinning. J. Membr. Sci. 370 (1-2), 124-130.

Meng, X., Liu, Z., Deng, C., Zhu, M., Wang, D., Li, K., Deng, Y., Jiang, M., 2016. Microporous nano-MgO/diatomite ceramic membrane with high positive surface charge for tetracycline removal. J. Hazard. Mater. 320, 495-503.

Nandi, B., Moparthi, A., Uppaluri, R., Purkait, M., 2010. Treatment of oily wastewater using low cost ceramic membrane: comparative assessment of pore blocking and artificial neural network models. Chem. Eng. Res. Des. 88 (7), 881-892.

Salahi, A., Gheshlaghi, A., Mohammadi, T., Madaeni, S.S., 2010. Experimental performance evaluation of polymeric membranes for treatment of an industrial oily wastewater. Desalination 262 (1-3), 235-242.

Shih, K., Tang, Y., 2011. Prolonged toxicity characteristic leaching procedure for nickel and copper aluminates. J. Environ. Monitor. 13 (4), 829-835.

Shih, K., White, T., Leckie, J.O., 2006a. Nickel stabilization efficiency of aluminate and ferrite spinels and their leaching behavior. Environ. Sci. Technol. 40 (17), 5520-5526.

Shih, K., White, T., Leckie, J.O., 2006b. Spinel formation for stabilizing simulated nickel-laden sludge with aluminum-rich ceramic precursors. Environ. Sci. Technol. 40 (16), 5077-5083.

Tang, Y., Chui, S.S.-Y., Shih, K., Zhang, L., 2011a. Copper stabilization via spinel formation during the sintering of simulated copper-laden sludge with aluminum-rich ceramic precursors. Environ. Sci. Technol. 45 (8), 3598-3604.

Tang, Y., Shih, K., Wang, Y., Chong, T.-C., 2011b. Zinc stabilization efficiency of aluminate spinel structure and its leaching behavior. Environ. Sci. Technol. 45 (24), 10544-10550.

Um, I.C., Kweon, H., Lee, K.G., Ihm, D.W., Lee, J.-H., Park, Y.H., 2004. Wet spinning of silk polymer: I. Effect of coagulation conditions on the morphological feature of filament. Int. J. Biol. Macromol. 34 (1-2), 89-105.

Vasanth, D., Pugazhenthi, G., Uppaluri, R., 2013. Cross-flow microfiltration of oil-in-water emulsions using low cost ceramic membranes. Desalination 320, 86-95.

Wang, D., Li, K., Teo, W., 2000. Highly permeable polyethersulfone hollow fiber gas separation membranes prepared using water as non-solvent additive. J. Membr. Sci. 176 (2), 147-158.

Zhang, X., Hu, J., Chang, Q., Wang, Y., Zhou, J.-e., Zhao, T., Jiang, Y., Liu, X., 2015. Influences of internal coagulant composition on microstructure and properties of porous YSZ hollow fibre membranes for water treatment. Sep. Purif. Technol. 147, 337-345.

Zhu, L., Chen, M., Dong, Y., Tang, C.Y., Huang, A., Li, L., 2016. A low-cost mullite-titania composite ceramic hollow fiber microfiltration membrane for highly efficient separation of oil-in-water emulsion. Water Res. 90, 277-285.